

Ultraconfined Plasmonic Hotspots Inside Graphene Nanobubbles

Z. Fei,^{*†‡§} J. J. Foley, IV,^{‡,||} W. Gannett,^{¶,#} M. K. Liu,^{†,||} S. Dai,[†] G. X. Ni,[†] A. Zettl,^{¶,#} M. M. Fogler,[†] G. P. Wiederrecht,[‡] S. K. Gray,[‡] and D. N. Basov^{‡,□}

[†]Department of Physics, University of California, San Diego, La Jolla, California 92093, United States

[‡]Center for Nanoscale Materials, Argonne National Laboratory, Argonne, Illinois 60439, United States

[§]Department of Physics and Astronomy, Iowa State University, Ames, Iowa 50011, United States

^{||}Department of Chemistry, William Paterson University, Wayne, New Jersey 07470, United States

[#]Department of Physics, University of California at Berkeley, Berkeley, California 94720, United States

[¶]Materials Sciences Division, Lawrence Berkeley National Laboratory, Berkeley, California 94720, United States

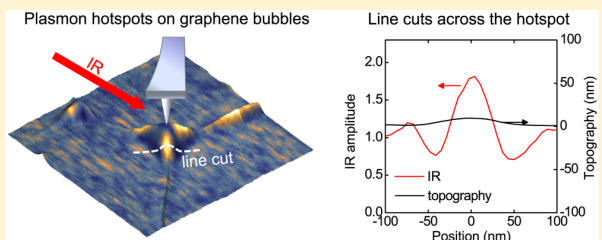
^{||}Department of Physics and Astronomy, Stony Brook University, Stony Brook, New York 11794, United States

[□]Department of Physics, Columbia University, New York, New York 10027, United States

Supporting Information

ABSTRACT: We report on a nano-infrared (IR) imaging study of ultraconfined plasmonic hotspots inside graphene nanobubbles formed in graphene/hexagonal boron nitride (hBN) heterostructures. The volume of these plasmonic hotspots is more than one-million-times smaller than what could be achieved by free-space IR photons, and their real-space distributions are controlled by the sizes and shapes of the nanobubbles. Theoretical analysis indicates that the observed plasmonic hotspots are formed due to a significant increase of the local plasmon wavelength in the nanobubble regions. Such an increase is attributed to the high sensitivity of graphene plasmons to its dielectric environment. Our work presents a novel scheme for plasmonic hotspot formation and sheds light on future applications of graphene nanobubbles for plasmon-enhanced IR spectroscopy.

KEYWORDS: Graphene nanobubbles, heterostructures, nano-infrared imaging, plasmon hotspots, FDTD simulation



Plasmonic hotspots are specific surface regions of metallic nanostructures where the plasmon field is highly confined in real space and thus becomes strongly enhanced in intensity.^{1–11} They attracted broad research interest in the context of both fundamental physics related to high-field electrodynamics^{4,5} as well as technological applications in biosensing^{6–8} and surface enhanced Raman/infrared (IR) spectroscopy.^{8–11} So far, studies of plasmonic hotspots are focused on noble metal based nanostructures where plasmons are normally in the visible or near-ultraviolet frequency range. Here we report on real-space nanoimaging of plasmonic hotspots in graphene, a novel plasmonic material that supports IR plasmons with high confinement, long lifetimes, electrostatic tunability, and propensity toward forming hybrid modes with other polaritons in two-dimensional van der Waals heterostructures.^{12–44} The observed hotspots reside in graphene nanobubbles^{40,45–49} that are mass-produced by transferring chemical-vapor-deposited graphene films⁵⁰ onto the hexagonal boron nitride (hBN) substrates^{51,52} followed by a standard thermal annealing process. As introduced in the Supporting Information, the nanobubbles could possibly encapsulate a mixture of air, water, or hydrocarbons that originate from the graphene transfer and annealing processes.^{45–49} Prior to our

research, these unique nanobubbles have served as platforms for studying the strain effects⁴⁸ and elastic properties⁴⁹ of graphene as well as the plasmon–phonon coupling phenomena⁴⁰ of the graphene/hBN heterostructure.

The IR nanoscope we utilized for nano-IR imaging is illustrated in Figure 1, panel a, where the IR light (solid arrow) from a continuous-wave laser is focused at a metallized tip of an atomic force microscope (AFM). The IR-illuminated sharp AFM tip acts as both a launcher and a detector of surface plasmon polaritons.^{30–44} The backscattered light (dashed arrow) off the tip–graphene system contains essential information about plasmons underneath the tip. The nanoscope collects simultaneously the AFM topography and near-field scattering amplitude (s). As demonstrated in previous studies,^{30–44} s is a reliable measure of the out-of-plane electric field amplitude (E_z) underneath the tip. In Figure 1, panel a, we plot an image of three-dimensional topography for a typical sample, where two graphene nanobubbles (labeled as "A" and

Received: September 29, 2016

Revised: November 8, 2016

Published: November 10, 2016

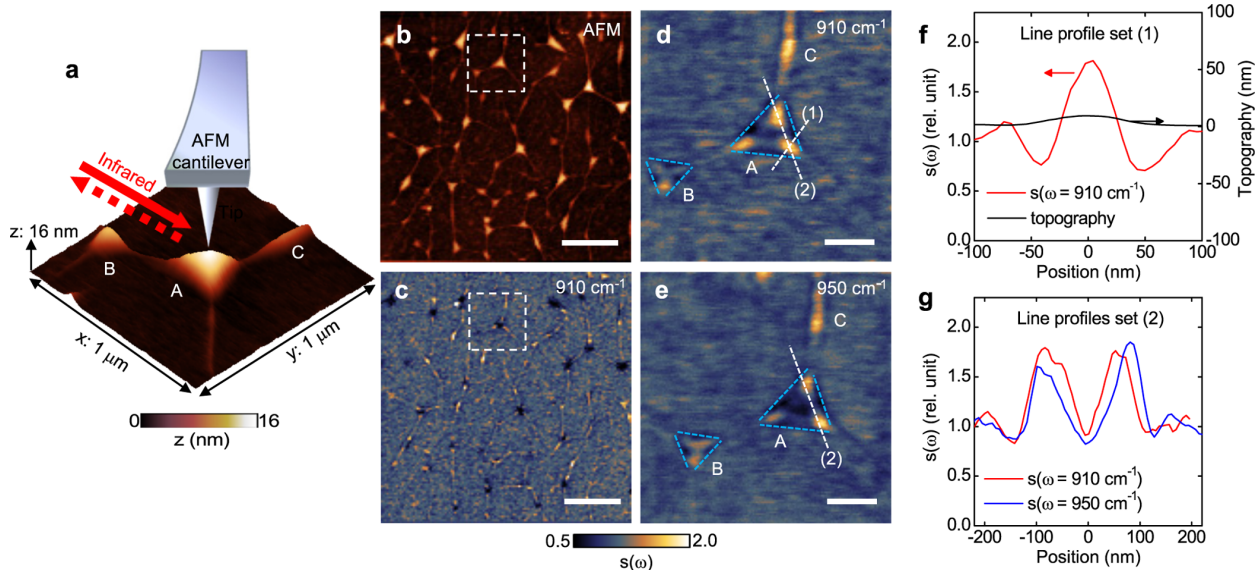


Figure 1. Nano-IR imaging of graphene nanobubbles revealing plasmonic hotspots. (a) Illustration of the nano-IR imaging experiment of graphene nanobubbles. Underneath the IR-illuminated tip lies a three-dimensional AFM topography image that reveals graphene nanobubbles. (b, c) Topography and nano-IR images of a large sample area that reveals tens of nanobubbles. The dashed squares here mark the sample area imaged in panel a. (d, e) Nano-IR images of the same sample area as in panel a taken at $\omega = 910$ and 950 cm^{-1} , respectively. The boundaries of the nanobubbles are marked with blue dashed lines. (f) Line profiles about both topography (black) and IR amplitude (red) across the hotspots along white dashed line (1) in panel d. (g) Line profiles of IR amplitude across two hotspots along white dashed line (2) in panels d and e. The false color in panels c–e denotes IR amplitude. Scale bars in panels b and c represent $1\text{ }\mu\text{m}$. Scale bars in panels d and e represent 200 nm .

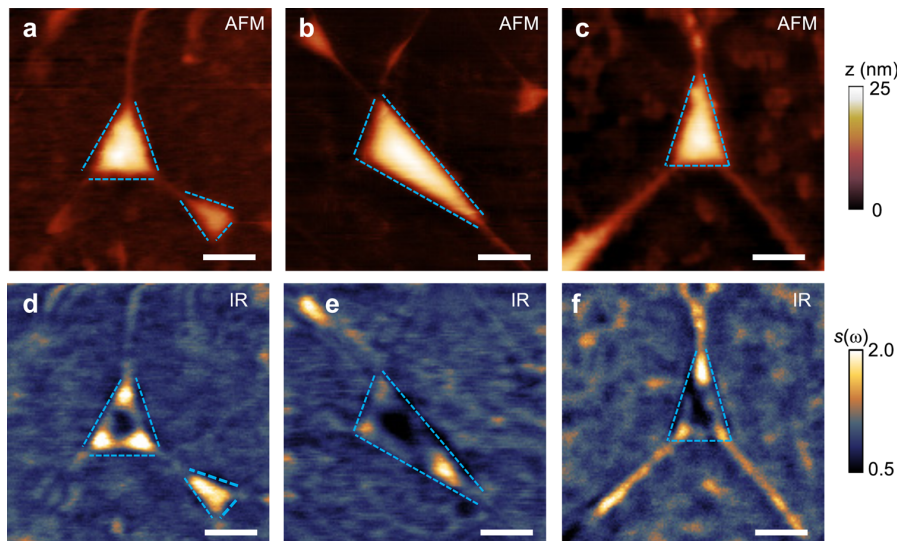


Figure 2. (a–c) AFM topography and (d–f) simultaneously taken nano-IR images of several graphene nanobubbles that reveal plasmonic hotspots. The excitation laser frequency is set to be $\omega = 910\text{ cm}^{-1}$. In all images, we mark the boundaries of the nanobubbles with blue dashed lines. Scale bars in all panels represent 200 nm .

“B”) can be clearly visualized. Both nanobubbles are pyramid-shaped with a triangular base. The lengths of the bottom edges (L) of the bubble A are about 250 nm with a height (H) of less than 20 nm . Bubble B has a smaller size in all dimensions compared to A. For both A and B, the aspect ratios (H/L) are below 0.1, which indicate relatively shallow topographic curvature of these bubbles. Such small aspect ratios apply to all other nanobubbles we found on our samples. As an example, we show a large-area scan with tens of nanobubbles densely

distributed in the sample area (Figure 1b). Among all these bubbles, the majority reveals the pyramidal shape. In addition to these bubbles, we can also see a number of wrinkles that connect one bubble to another throughout the map. The nano-IR image simultaneously taken with Figure 1, panel b is plotted in Figure 1, panel c where one can see many bright hotspots within the sample area.

To reveal the details of these hotspots, we show in Figure 1, panel d a zoomed-in nano-IR image that is in the same sample

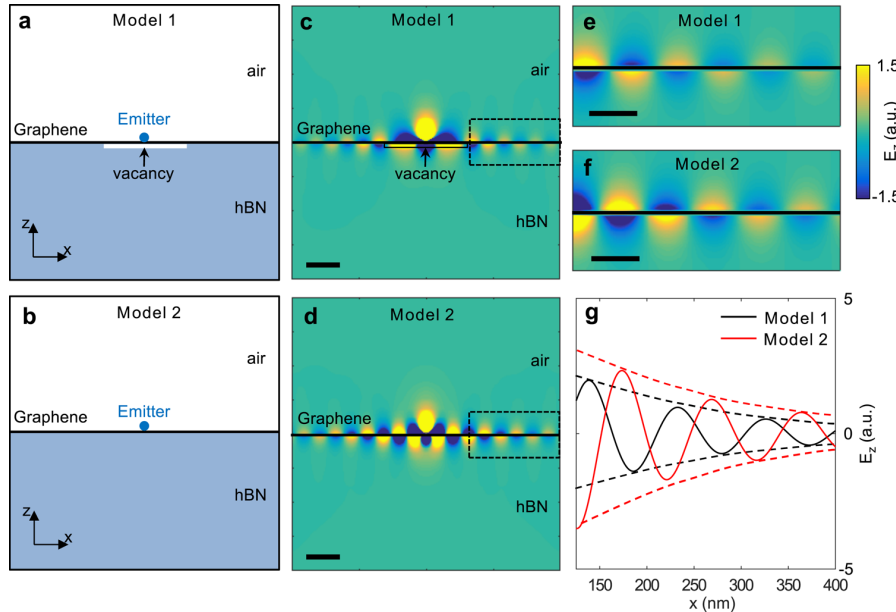


Figure 3. FDTD simulations of surface plasmon polaritons launched by a point emitter above graphene on hBN. (a) Model 1: graphene on a cylinder vacancy (depth = 10 nm; diameter = 250 nm) in hBN filled with a uniform media with a permittivity of $\epsilon \approx 1$ to simulate the dielectric environment of air or hydrocarbon gas inside nanobubbles. (b) Model 2: graphene on an intact hBN substrate. (c, d) Simulated E_z maps of Model 1 and Model 2, respectively. (e, f) Zoomed-in E_z maps of the regions defined by the dashed rectangles in panels c and d, respectively. (g) Horizontal line profiles of E_z taken right above the graphene surface in panels e and f. Scale bars represent 100 nm in panels c and d, and represent 50 nm in panels e and f.

area as Figure 1, panel a. The excitation laser frequency was set to $\omega = 910 \text{ cm}^{-1}$ corresponding to a photon energy of 113 meV. Here multiple hotspots are clearly located inside these bubbles. We first discuss the bubble A at the center of the image, where three hotspots are distributed close to the corners of the pyramid. In Figure 1, panel f, we plot the line profiles for both topography (black curve) and IR amplitude (red curve) across one of the hotspots along the dashed line (1) in Figure 1, panel d. From Figure 1, panel f, one can see that the IR amplitude nearly doubles at the center of the hotspot despite a minute topographic variation of less than 10 nm. Moreover, the IR amplitude peak of the hotspot has a full-width at half-maximum (W) of $\sim 50 \text{ nm}$, which indicates that the hotspot is highly localized in real space compared to the excitation IR wavelength ($\lambda_{\text{IR}} \approx 11 \mu\text{m}$). Consequently, the mode volume ($\sim W^3$) is more than one-million-times smaller than what could be achieved by free-space IR photons ($\sim \lambda_{\text{IR}}^3$). In Figure 1, panel e, we plot the nano-IR image taken at $\omega = 950 \text{ cm}^{-1}$ in the same sample area as Figure 1, panel d. Compared to Figure 1, panel d, we find that the three hotspots of bubble A in Figure 1, panel e move toward the corners of the bubble. As a result, the separations between hotspots increase at $\omega = 950 \text{ cm}^{-1}$. This can be seen more clearly in Figure 1, panel g, where we plot the extracted line profiles along dashed lines (2) that connect two hotspots (Figure 1d,e). The observed frequency dependence is consistent with the plasmonic origin of these hotspots (Figure S6).

In addition to the nanobubble A, hotspots are also seen inside the nanobubble B (Figure 1d,e). There are also three hotspots in B, but they are much closer toward the center, barely distinguishable from each other. We provide additional nanoimaging data of various nanobubbles in Figure 2. In general, for large pyramid-shaped bubbles, the hotspots

normally reside at the corners, while for small bubbles they tend to appear at the center. In all cases, the hotspots are highly confined in space with strong field enhancement. Note that hotspots were also seen frequently inside wrinkles with sizable widths and heights (Figure 1d,e and Figure 2). For example, the wrinkle at location C in Figure 1, panel a with a width of $\sim 100 \text{ nm}$ and a height of $\sim 6 \text{ nm}$ has a hotspot at the center.

We assert that the observed hotspots are formed due to the localization of tip-excited graphene plasmons inside the graphene nanobubbles or wide wrinkles. We are able to reproduce the hotspot patterns as well as their dependences with the bubble size or the plasmon wavelength through real-space simulations assuming mode localization effects (Figure S6). Plasmonic hotspots were also observed previously in patterned graphene nanostructures,^{30,31,34,41} where localization of the plasmonic energy is due to the termination of graphene at the edges. In the case of graphene nanobubbles, the plasmon localization occurs due to the impedance mismatch at the boundaries between graphene nanobubbles and flat graphene region (blue dashed curves in Figures 1 and 2).

We now elaborate on two possible causes of impedance mismatch that are responsible for the plasmon localization and hence the hotspot formation inside the nanobubbles. One is the variation of topography, and the other is the change of the local plasmon wavevector (q_p). Under the Drude approximation, q_p can be written as

$$q_p = \frac{\hbar \kappa(\omega)}{2e^2 v_F \sqrt{\pi |n|}} \omega(\omega + i\Gamma) \quad (1)$$

where $\kappa(\omega)$, v_F , n , and Γ are the effective dielectric function of environment, Fermi velocity, charge density, and charge scattering rate of graphene, respectively.³⁰ On the basis of eq 1, it can be seen that $\kappa(\omega)$, v_F , n , and Γ are the main parameters

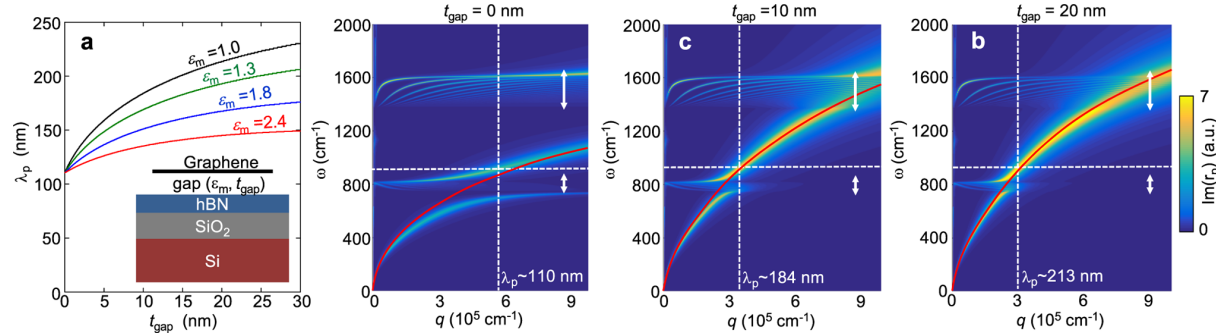


Figure 4. Theoretical calculations of the local plasmon wavelength (λ_p) and dispersion diagrams of a modeled heterostructure. (a) Calculated λ_p versus gap size t_{gap} . We consider a homogeneous gap medium with a dielectric constant of $\epsilon_m = 1.0$ to 2.4 (see Supporting Information for discussions about the filling materials inside the bubble). Inset plots the modeled heterostructure for the calculation. (b-d) Calculated frequency (ω)–momentum (q) dispersion diagrams for all polariton modes in the heterostructure system considering $\epsilon_m = 1$. The white arrows in panels b–d mark the two reststrahlen bands 746–819 cm⁻¹ and 1370–1610 cm⁻¹ of hBN where graphene plasmons couple strongly with hyperbolic phonon polaritons in hBN. The red curves mark the plasmon dispersion without consideration of phonon polaritons in hBN. The horizontal and vertical dashed lines in panels b–d mark the excitation frequency ($\omega = 910$ cm⁻¹) and corresponding plasmon wave vectors of graphene.

that control q_p . It is well-known that hBN is an ideal substrate that contributes little doping or scattering to graphene.⁵² Therefore, it is safe to rule out the possibility that n and Γ on top of the graphene bubbles are consistently and largely different from the flat graphene/hBN region. The Fermi velocity (v_F) scales with graphene strain.⁵³ The strain effects of graphene nanobubbles on hBN have been studied in an earlier work,⁴⁸ where it was found that thermal annealing induces isotropic compressive strain in the flat graphene/hBN region and the strain is released in the bubble region. The induced compressive strain, which scales with the annealing temperature, is estimated to be about 0.06% in our samples.⁴⁸ Such a tiny strain will have negligible effects on v_F and hence the plasmonic properties of graphene.⁵³

To evaluate the effects of topography and dielectric environment on graphene plasmons, we performed two control simulations with the finite difference time domain (FDTD) method. In one case, we study suspended graphene with a nanobubble at the center (Figure S5) to evaluate the effects of topographic curvature on graphene plasmons. For simplicity, we consider a Gaussian-shaped bubble in our simulation. The radius of curvature ($R_{bubble} \approx 600$ nm) of the modeled bubble is comparable to that of the bubbles in our experiment (Figure 1). As shown in Figure S5, graphene plasmons can propagate almost freely off the bubble with negligible energy loss despite the curvature. Such an observation is attributed to the high spatial confinement of graphene plasmons that leads to little radiation loss on curved graphene.⁵⁴ Indeed, the plasmon wavelength (λ_p) is in the range of 100–200 nm (see discussions below) that is far smaller than R_{bubble} . Therefore, we are safe to conclude that the minute topographic variations of our nanobubbles are not responsible for the hotspots formation inside the bubbles.

We also investigate flat graphene on an hBN substrate where a cylindrical vacancy sits at the center of the substrate (Model 1, Figure 3a). More detailed sketches about the geometric shape, orientation, and aspect ratio of the vacancy are shown in Figure S2, where we plot the 3D side view (Figure S2a), the x – y plane top view (Figure S2b), and the x – z plane cross-sectional view (Figure S2c) of the hBN substrate together with the cylindrical vacancy. With this simplified model, we are able to simulate the dielectric environment of the nanobubbles in

our experiments without introducing topographic variations. As an example, we consider a homogeneous distribution of a dielectric medium with a permittivity of $\epsilon_m = 1$ inside the vacancy to simulate the environment of air or hydrocarbon gas. The general effect will be similar when considering other possible media (e.g., water or other forms of hydrocarbons) inside the bubbles as discussed in detail in the Supporting Information. The depth and diameter of the cylindrical vacancy is set to be 10 nm (about average height of the bubble) and 250 nm to match the aspect ratio of nanobubble A in Figure 1. A point-dipole plasmon emitter is placed right above the vacancy in close proximity to graphene. As a control, we also performed simulations of flat graphene on an intact hBN substrate (Model 2, Figure 3b).

The simulation results are shown in Figure 3, panels c and d, where we plot the cross-sectional (x – z plane across the emitter) snapshots of the z -component of the electric field (E_z). One can see that in both Figure 3, panels c and d graphene plasmons launched by the emitter propagate away along the graphene plane. Here, we normalize the field right underneath the emitter and compare the region a few plasmon wavelengths away from the emitter (marked with dashed rectangles in Figure 3c,d) where graphene plasmons are the dominant source of electric field. In Figure 3, panels e and f, we plot the zoomed-in views of the rectangle regions, which show notable differences in both the amplitude and phase of the plasmon field in model 1 compared to model 2. A quantitative comparison of the two models is presented in Figure 3, panel g, where we took line profiles of E_z right above graphene from Figure 3, panels e and f. One can see clearly that the field amplitude ($|E_z|$) of graphene plasmons propagating away from the vacancy region (black curve) is about 30% less compared to that on the flat hBN substrate (red curves), which indicates a plasmonic transmittance of $T = (1 - 30\%)^2 \approx 50\%$ at the boundary of the vacancy. Considering the huge momentum mismatch between plasmons and IR photons, the direct plasmon-to-photon emission should be negligible,⁵⁴ so the plasmonic reflectance ($R \approx 1 - T$) at the vacancy boundary is also estimated to be close to 50%. Such a sizable plasmon reflectance is responsible for the confinement of the plasmonic energy inside the vacancy/bubble region.

The FDTD simulations discussed above suggest that the variation of dielectric environment is a likely cause for the impedance mismatch between nanobubbles and flat graphene on hBN. The physical origin behind the impedance mismatch, as detailed below, is a significant increase of the local plasmon wavelength (λ_p) on top the graphene nanobubbles. To determine λ_p , we first calculate the plasmon dispersion considering the entire graphene/gap/substrate system (inset of Figure 4a). The added gap region here is to simulate the dielectric medium inside the graphene nanobubbles. Details of the calculations are introduced in the Supporting Information. The gap layer here between graphene and hBN is filled with a uniform medium with a dielectric constant of ϵ_m . Here in the dispersion color plots (Figure 4b–d), ϵ_m is set to be 1, and the thickness of the gap layer (t_{gap}) varies from 0 to 20 nm. The bright curves in the dispersion color plots represent various surface modes of our system. One can see that the intrinsic graphene plasmon mode (with $q^{1/2}$ scaling, marked with red curves) coupled strongly with the hBN hyperbolic phonon waveguide modes in the two reststrahlen bands $746\text{--}819\text{ cm}^{-1}$ and $1370\text{--}1610\text{ cm}^{-1}$ (within the ranges defined by the white arrows).^{36,55–59} To avoid the strong coupling regions, we chose excitation frequencies away from the two reststrahlen bands. For example, the horizontal dashed lines in Figure 4, panels b–d mark the frequency of $\omega = 910\text{ cm}^{-1}$, where the response is predominantly plasmonic. The cross-points between the horizontal dashed lines and the graphene plasmon mode determine the plasmon wavevector q_p (vertical dashed line); hence, the plasmon wavelength $\lambda_p \approx 2\pi/q_p$ at this frequency. With this method, we are able to plot the complete $t_{\text{gap}}-\lambda_p$ dependence curve at $\omega = 910\text{ cm}^{-1}$ assuming $\epsilon_m = 1$ (Figure 4a, black curve). In Figure 4, panel a, we also plot the calculated dependence curves considering $\epsilon_m = 1.3$, 1.8, and 2.4 corresponding to other possible filling materials (Supporting Information). In all cases, the plasmon wavelength increases with t_{gap} , which is due to the relatively lower values of ϵ_m compared to the effective dielectric constant of hBN ($\epsilon_{\text{eff}} \approx 4.0$) at $\omega = 910\text{ cm}^{-1}$ (Supporting Information). The increase of the local plasmon wavelength can also be seen by comparing FDTD simulations of Model 1 and Model 2 (see Figure 3c,d and their zoomed-in snapshots in Figure S4b,d). These simulated field maps reveal a larger mode period of graphene plasmons above the vacancy region compared to that on the flat hBN substrate, which is a direct evidence of the strong sensitivity of graphene plasmons to its dielectric environment.

Our nano-IR imaging experiments establish graphene nanobubbles on hBN substrates as an effective plasmonic cavity for trapping plasmons with subhundred-nanometer spatial confinement. These highly confined hotspots are ideal for plasmon-enhanced IR spectroscopy of nanoscale objects. Of particular interest are biomolecules whose IR vibration modes could be significantly enhanced by electrostatically tunable graphene plasmons.^{60,61} Moreover, graphene nanobubbles are perfect for encapsulating biomolecules in an aqueous environment.^{62–64} Therefore, one can in principle monitor structural changes of molecules upon growth inside these nanobubbles. Our study sheds light on future applications of graphene nanobubbles for plasmon-enhanced IR spectroscopy of biomolecules.

■ ASSOCIATED CONTENT

§ Supporting Information

The Supporting Information is available free of charge on the ACS Publications website at DOI: [10.1021/acs.nanolett.6b04076](https://doi.org/10.1021/acs.nanolett.6b04076).

Details of experiments, calculations, and simulations (PDF)

■ AUTHOR INFORMATION

Corresponding Author

*E-mail: zfei@iastate.edu.

ORCID

Z. Fei: [0000-0002-7940-5566](https://orcid.org/0000-0002-7940-5566)

J. J. Foley, IV: [0000-0001-8814-4444](https://orcid.org/0000-0001-8814-4444)

Notes

The authors declare no competing financial interest.

■ ACKNOWLEDGMENTS

Authors acknowledge support from ONR and AFOSR. The development of scanning plasmon interferometry is supported by ARO. D.N.B. is supported by the Gordon and Betty Moore Foundation's EPiQS Initiative through Grant No. GBMF4533. M.M.F. is supported by UCOP. Theory and analysis work was performed, in part, at the Center for Nanoscale Materials, a U.S. Department of Energy Office of Science User Facility under Contract No. DE-AC02-06CH11357.

■ REFERENCES

- (1) Lahiri, B.; Holland, G.; Aksyuk, V.; Centrone, A. *Nano Lett.* **2013**, *13* (7), 3218–3224.
- (2) Valev, V. K.; Silhanek, A. V.; Jeyaram, Y.; Denkova, D.; De Clercq, B.; Petkov, V.; Zheng, X.; Volskiy, V.; Gillijns, W.; Vandenbosch, G. A. E.; Aktsipetrov, O. A.; Ameloot, M.; Moshchalkov, V. V.; Verbiest, T. *Phys. Rev. Lett.* **2011**, *106*, 226803.
- (3) Cang, H.; Labno, A.; Lu, C.; Yin, X.; Liu, M.; Gladden, C.; Liu, Y.; Zhang, X. *Nature* **2011**, *469*, 385–388.
- (4) Abb, M.; Wang, Y.; de Groot, C. H.; Muskens, O. L. *Nat. Commun.* **2014**, *5*, 4869.
- (5) Harutyunyan, H.; Martinson, A. B.F.; Rosenmann, D.; Khorashad, L. K.; Besteiro, L. V.; Govorov, L. O.; Wiederrecht, G. P. *Nat. Nanotechnol.* **2015**, *10*, 770–774.
- (6) Brolo, A. G. *Nat. Photonics* **2012**, *6*, 709–713.
- (7) Zhang, N.; Liu, Y. J.; Yang, J.; Su, X.; Deng, J.; Chum, C. C.; Hong, M.; Teng, J. *Nanoscale* **2014**, *6*, 1416–1422.
- (8) Camden, J. P.; Dieringer, J. A.; Zhao, J.; Van Duyne, R. P. *Acc. Chem. Res.* **2008**, *41*, 1653–1661.
- (9) Ertsgaard, C. T.; McKoskey, R. M.; Rich, I. S.; Lindquist, N. C. *ACS Nano* **2014**, *8* (10), 10941–10946.
- (10) Wei, H.; Xu, H. *Nanoscale* **2013**, *5*, 10794–10805.
- (11) Chen, G.; Wang, Y.; Yang, M.; Xu, J.; Goh, S. J.; Pan, M.; Chen, H. *J. Am. Chem. Soc.* **2010**, *132* (11), 3644–3645.
- (12) Basov, D. N.; Fogler, M. M.; García de Abajo, F. J. *Science* **2016**, *354*, 195.
- (13) Crassee, I.; Orlita, M.; Potemski, M.; Walter, A. L.; Ostler, M.; Seyller, T.; Gaponenko, I.; Chen, J.; Kuzmenko, A. B. *Nano Lett.* **2012**, *12* (5), 2470–2474.
- (14) Vakil, A.; Engheta, N. *Science* **2011**, *332*, 1291–1294.
- (15) Koppens, F. H. L.; Chang, D. E.; Garcia de Abajo, F. J. *Nano Lett.* **2011**, *11* (8), 3370–3377.
- (16) Grigorenko, A. N.; Polini, M.; Novoselov, K. S. *Nat. Photonics* **2012**, *6*, 749–758.
- (17) Bao, Q.; Loh, K. P. *ACS Nano* **2012**, *6* (5), 3677–3694.
- (18) Basov, D. N.; Fogler, M. M.; Lanzara, A.; Wang, F.; Zhang, Y. *Rev. Mod. Phys.* **2014**, *86*, 959–994.

- (19) Ju, L.; Geng, B.; Horng, J.; Girit, C.; Martin, M.; Hao, Z.; Bechtel, H. A.; Liang, X.; Zettl, A.; Shen, Y. R.; Wang, F. *Nat. Nanotechnol.* **2011**, *6*, 630–634.
- (20) Yan, H.; Li, X.; Chandra, B.; Tulevski, G.; Wu, Y.; Freitag, M.; Zhu, W.; Avouris, P.; Xia, F. *Nat. Nanotechnol.* **2012**, *7*, 330–334.
- (21) Brar, V. W.; Jang, M. S.; Sherrott, M.; Lopez, J. J.; Atwater, H. A. *Nano Lett.* **2013**, *13*, 2541–2547.
- (22) Fang, Z.; Thongrattanasiri, S.; Schlather, A.; Liu, Z.; Ma, L.; Wang, Y.; Ajayan, P.; Nordlander, P.; Halas, N. J.; Garcia de Abajo, F. J. *ACS Nano* **2013**, *7* (3), 2388–2395.
- (23) Gao, W.; Shi, G.; Jin, Z.; Shu, J.; Zhang, Q.; Vajtai, R.; Ajayan, P. M.; Kono, J.; Xu, Q. *Nano Lett.* **2013**, *13*, 3698–3702.
- (24) Yan, H.; Low, T.; Zhu, W.; Wu, Y.; Freitag, M.; Li, X.; Guinea, F.; Avouris, P.; Xia, F. *Nat. Photonics* **2013**, *7*, 394–399.
- (25) Strait, J. H.; Nene, P.; Chan, W.-M.; Manolatou, C.; Tiwari, S.; Rana, F.; Kevek, J. W.; McEuen, P. L. *Phys. Rev. B: Condens. Matter Mater. Phys.* **2013**, *87*, 241410R.
- (26) Poumirol, J. M.; Yu, W.; Chen, X.; Berger, C.; de Heer, W. A.; Smith, M. L.; Ohta, T.; Pan, W.; Goerbig, M. O.; Smirnov, D.; Jiang, Z. *Phys. Rev. Lett.* **2013**, *110*, 246803.
- (27) Fang, Z.; Wang, Y.; Schlather, A. E.; Liu, Z.; Ajayan, P. M.; Garcia de Abajo, F. J.; Nordlander, P.; Zhu, X.; Halas, N. J. *Nano Lett.* **2014**, *14* (1), 299–304.
- (28) Fei, Z.; Andreev, G. O.; Bao, W.; Zhang, L. M.; McLeod, A. S.; Wang, C.; Stewart, M. K.; Zhao, Z.; Dominguez, G.; Thiemens, M.; Fogler, M. M.; Tauber, M. J.; Castro-Neto, A. H.; Lau, C. N.; Bockrath, M.; Basov, D. N. *Nano Lett.* **2011**, *11*, 4701–4705.
- (29) Wagner, M.; Fei, Z.; McLeod, A. S.; Rodin, A. S.; Bao, W.; Iwinski, E. G.; Zhao, Z.; Goldflam, M.; Liu, M. K.; Dominguez, G.; Thiemens, M.; Fogler, M. M.; Castro Neto, A. H.; Lau, C. N.; Amaric, S.; Keilmann, F.; Basov, D. N. *Nano Lett.* **2014**, *14*, 894–900.
- (30) Fei, Z.; Rodin, A. S.; Andreev, G. O.; Bao, W.; McLeod, A. S.; Wagner, M.; Zhang, L. M.; Zhao, Z.; Thiemens, M.; Dominguez, G.; Fogler, M. M.; Castro Neto, A. H.; Lau, C. N.; Keilmann, F.; Basov, D. N. *Nature* **2012**, *487*, 82–85.
- (31) Chen, J.; Badioli, M.; Alonso-González, P.; Thongrattanasiri, S.; Huth, F.; Osmond, J.; Spasenović, M.; Centeno, A.; Pesquera, A.; Godignon, P.; Elorza, A. Z.; Camara, N.; García de Abajo, F. J.; et al. *Nature* **2012**, *487*, 77–81.
- (32) Fei, Z.; Rodin, A. S.; Gannett, W.; Dai, S.; Regan, W.; Wagner, M.; Liu, M. K.; McLeod, A. S.; Dominguez, G.; Thiemens, M.; Castro Neto, A. H.; Keilmann, F.; Zettl, A.; Hillenbrand, R.; Fogler, M. M.; Basov, D. N. *Nat. Nanotechnol.* **2013**, *8*, 821–825.
- (33) Alonso-González, P.; Nikitin, A. Y.; Golmar, F.; Centeno, A.; Pesquera, A.; Velez, S.; Chen, J.; Navickaitė, G.; Koppens, F.; Zurutuza, A.; Casanova, F.; Hueso, L. E.; Hillenbrand, R. *Science* **2014**, *344*, 1369–1373.
- (34) Gerber, J. A.; Berweger, S.; O’Callahan, B. T.; Raschke, M. B. *Phys. Rev. Lett.* **2014**, *113*, 055502.
- (35) Woessner, G.; Lundeberg, M. B.; Gao, Y.; Principi, A.; Alonso-González, P.; Carrega, M.; Watanabe, K.; Taniguchi, T.; Vignale, G.; Polini, M.; Hone, J.; Hillenbrand, R.; Koppens, F. H. L. *Nat. Mater.* **2014**, *14*, 421–425.
- (36) Dai, S.; Ma, Q.; Liu, M. K.; Andersen, T.; Fei, Z.; Goldflam, M. D.; Wagner, M.; Watanabe, K.; Taniguchi, T.; Thiemens, M.; Keilmann, F.; Janssen, G. C. A. M.; Zhu, S.-E.; Jarillo-Herrero, P.; Fogler, M. M.; Basov, D. N. *Nat. Nanotechnol.* **2015**, *10*, 682–686.
- (37) Fei, Z.; Iwinski, E. G.; Ni, G. X.; Zhang, L. M.; Bao, W.; Rodin, A. S.; Lee, Y.; Wagner, M.; Liu, M. K.; Dai, S.; Goldflam, M. D.; Thiemens, M.; Keilmann, F.; Lau, C. N.; Castro-Neto, A. H.; Fogler, M. M.; Basov, D. N. *Nano Lett.* **2015**, *15*, 4973–4978.
- (38) Ni, G. X.; Wang, H.; Wu, J. S.; Fei, Z.; Goldflam, M. D.; Keilmann, F.; Özyilmaz, B.; Castro Neto, A. H.; Xie, X. M.; Fogler, M. M.; et al. *Nat. Mater.* **2015**, *14*, 1217–1222.
- (39) Fei, Z.; Goldflam, M. D.; Wu, J.-S.; Dai, S.; Wagner, M.; McLeod, A. S.; Liu, M. K.; Post, K. W.; Zhu, S.; Janssen, G. C. A. M.; Fogler, M. M.; Basov, D. N. *Nano Lett.* **2015**, *15* (12), 8271–8276.
- (40) Barcelos, I. D.; Cadore, A. R.; Campos, L. C.; Malachias, A.; Watanabe, K.; Taniguchi, T.; Maia, F. C. B.; Freitas, R.; Deneke, C. *Nanoscale* **2015**, *7*, 11620–11625.
- (41) Nikitin, A. Y.; Alonso-González, P.; Vélez, S.; Mastel, S.; Centeno, A.; Pesquera, A.; Zurutuza, A.; Casanova, F.; Hueso, L. E.; Koppens, F. H. L.; Hillenbrand, R. *Nat. Photonics* **2016**, *10*, 239–243.
- (42) Ni, G. X.; Wang, L.; Goldflam, M. D.; Wagner, M.; Fei, Z.; McLeod, A. S.; Liu, M. K.; Keilmann, F.; Özyilmaz, B.; Castro Neto, A. H.; Hone, J.; Fogler, M. M.; Basov, D. N. *Nat. Photonics* **2016**, *10*, 244–247.
- (43) Yang, X.; Zhai, F.; Hu, H.; Hu, D.; Liu, R.; Zhang, S.; Sun, M.; Sun, Z.; Chen, J.; Dai, Q. *Adv. Mater.* **2016**, *28*, 2931–2938.
- (44) Jiang, B.-Y.; Ni, G. X.; Pan, C.; Fei, Z.; Cheng, B.; Lau, C. N.; Bockrath, M.; Basov, D. N.; Fogler, M. M. *Phys. Rev. Lett.* **2016**, *117*, 086801.
- (45) Mayorov, A. S.; Gorbachev, R. V.; Morozov, S. V.; Britnell, L.; Jalil, R.; Ponomarenko, L. A.; Blake, P.; Novoselov, K. S.; Watanabe, K.; Taniguchi, T.; Geim, A. K. *Nano Lett.* **2011**, *11* (6), 2396–2399.
- (46) Baart, T. A. *Quantum Dots on Bilayer Graphene Made on a Substrate of Boron Nitride Using Split Gates*, Ph.D. Thesis, Delft University of Technology, Delft, The Netherlands, 2011.
- (47) Haigh, S. J.; Gholinia, A.; Jalil, R.; Romani, S.; Britnell, L.; Elias, D. C.; Novoselov, K. S.; Ponomarenko, L. A.; Geim, A. K.; Gorbachev, R. *Nat. Mater.* **2012**, *11*, 764–767.
- (48) Pan, W.; Xiao, J.; Zhu, J.; Yu, C.; Zhang, G.; Ni, Z.; Watanabe, K.; Taniguchi, T.; Shi, Y.; Wang, X. *Sci. Rep.* **2012**, *2*, 893.
- (49) Khestanova, E.; Guinea, F.; Fumagalli, L.; Geim, A. K.; Grigorieva, I. V. *Nat. Commun.* **2016**, *7*, 12587.
- (50) Li, X.; Cai, W.; An, J.; Kim, S.; Nah, J.; Yang, D.; Piner, R.; Velamakanni, A.; Jung, I.; Tutuc, E.; Banerjee, S. K.; Colombo, L.; Ruoff, R. S. *Science* **2009**, *324*, 1312–1314.
- (51) Gannett, W.; Regan, W.; Watanabe, K.; Taniguchi, T.; Crommie, M. F.; Zettl, A. *Appl. Phys. Lett.* **2011**, *98*, 242105.
- (52) Dean, C. R.; Young, A. F.; Meric, I.; Lee, C.; Wang, L.; Sorgenfrei, S.; Watanabe, K.; Taniguchi, T.; Kim, P.; Shepard, K. L.; Hone, J. *Nat. Nanotechnol.* **2010**, *5*, 722–726.
- (53) Choi, S.-M.; Jhi, S.-H.; Son, Y.-W. *Phys. Rev. B: Condens. Matter Mater. Phys.* **2010**, *81*, 081407R.
- (54) Lu, W. B.; Zhu, W.; Xu, H. J.; Ni, Z. H.; Dong, Z. G.; Cui, T. J. *Opt. Express* **2013**, *21*, 10475–10482.
- (55) Dai, S.; Fei, Z.; Ma, Q.; Rodin, A. S.; Wagner, M.; McLeod, A. S.; Liu, M. K.; Gannett, W.; Regan, W.; Watanabe, K.; Taniguchi, T.; Thiemens, M.; Dominguez, G.; Castro Neto, A. H.; Zettl, A.; Keilmann, F.; Jarillo-Herrero, P.; Fogler, M. M.; Basov, D. N. *Science* **2014**, *343*, 1125–1129.
- (56) Caldwell, J. D.; Kretinin, A. V.; Chen, Y.; Giannini, V.; Fogler, M. M.; Francescato, Y.; Ellis, C. T.; Tischler, J. G.; Woods, C. R.; Giles, A. J.; Hong, M.; Watanabe, K.; Taniguchi, T.; Maier, S. A.; Novoselov, K. S. *Nat. Commun.* **2014**, *5*, 5221.
- (57) Dai, S.; Ma, Q.; Andersen, T.; Mcleod, A. S.; Fei, Z.; Liu, M. K.; Wagner, M.; Watanabe, K.; Taniguchi, T.; Thiemens, M.; Keilmann, F.; Jarillo-Herrero, P.; Fogler, M. M.; Basov, D. N. *Nat. Commun.* **2015**, *6*, 6963.
- (58) Li, P.; Lewin, M.; Kretinin, A. V.; Caldwell, J. D.; Novoselov, K. S.; Taniguchi, T.; Watanabe, K.; Gaussmann, F.; Taubner, T. *Nat. Commun.* **2015**, *6*, 7507.
- (59) Yoxall, E.; Schnell, M.; Nikitin, A. Y.; Txoperena, O.; Woessner, A.; Lundeberg, M. B.; Casanova, F.; Hueso, L. E.; Koppens, F. H. L.; Hillenbrand, R. *Nat. Photonics* **2015**, *9*, 674–678.
- (60) Li, Y.; Yan, H.; Farmer, D. B.; Meng, X.; Zhu, W.; Osgood, R. M.; Heinz, T. F.; Avouris, P. *Nano Lett.* **2014**, *14*, 1573–1577.
- (61) Rodrigo, D.; Limaj, O.; Janner, D.; Etezadi, D.; Garcia de Abajo, F. J.; Pruneri, V.; Altug, H. *Science* **2015**, *349*, 165–168.
- (62) Yuk, J. M.; Park, J.; Ercius, P.; Kim, K.; Hellebusch, D. J.; Crommie, M. F.; Lee, J. Y.; Zettl, A.; Alivisatos, A. P. *Science* **2012**, *336*, 61–64.
- (63) Xuan Lim, C. H. Y.; Sorkin, A.; Bao, Q.; Li, A.; Zhang, K.; Nesladek, M.; Loh, K. P. *Nat. Commun.* **2013**, *4*, 1556.

- (64) Khatib, O.; Wood, J. D.; McLeod, A. S.; Goldflam, M. D.; Wagner, M.; Damhorst, G. L.; Koepke, J. C.; Doidge, G. P.; Rangarajan, A.; Bashir, R.; Pop, E.; Lyding, J. W.; Thiemens, M. H.; Keilmann, F.; Basov, D. N. *ACS Nano* **2015**, *9*, 7968–775.